Uncertainty quantification of solute transport coefficients

4

Ravi Agarwal, Dallas R. Trinkle
Department of Materials Science and Engineering, University of Illinois at Urbana-Champaign, Urbana, IL, United States

4.1 Introduction

Diffusion in crystals is a fundamental defect-driven process leading to transport of solutes via interstitial- or vacancy-mediated mechanisms [1]. Diffusion controls a variety of phenomena in materials including ion transport, irradiation-induced degradation of materials, recrystallization, and the formation and growth of precipitates [2]. Transport coefficients are fundamental inputs for models at the length and time scales of microstructure evolution. Accurate knowledge of transport coefficients can aid in the design of novel alloys via an integrated computational materials engineering approach. Experimental determination of transport coefficients rely on measurements of solute concentration profiles of tracers using serial sectioning, residual activity, or secondary ion mass spectroscopy analysis. Generally, these experimental measurements are accessible only for limited temperatures and can require large investments in time and resources to generate a transport database. Diffusion modeling coupled with first-principles data is a promising alternate strategy to generate a database of transport coefficients over a broad temperature range [3−5], similar to the role that computational thermodynamics has played in the development of phase diagrams.

The accuracy of computed transport coefficients is affected from the approximations made in the diffusion model [6−8] as well as the uncertainties inherent to first-principles calculations [3,9,10]. Agarwal and Trinkle showed that an approximate treatment of vacancy correlations in the vacancy-mediated transport of solutes lead to an overestimation of 100 meV in the activation energy of diffusion [8]. The computationally efficient Green's function (GF) approach removes approximations associated with the correlation in defect trajectories to compute exact transport coefficients for interstitial and vacancy-mediated diffusion in the *dilute limit* of solute [11]. The GF approach can also enable uncertainty quantification of transport coefficients by propagating uncertainty from the density functional theory (DFT) data. In DFT, the treatment of electron's exchange and correlation (XC) can be approximated with different approaches. Medasani et al. [9] and Shang et al. [10] systematically computed the vacancy formation energy and vacancy migration barrier in bulk lattices for various XC functionals and showed that these energies vary significantly across different functionals. Shang et al. [10] also computed the self-diffusion

coefficients for 82 pure elements for four different XC functionals but a comprehensive methodology to quantify uncertainty in diffusion coefficients is missing. Currently, there are no published theoretical studies to quantify uncertainty for vacancy-mediated solute transport coefficients, and compare with experimental studies.

This chapter presents a methodology based on a Bayesian framework to quantify uncertainties in transport coefficients, applied to a transport database for 61 solutes in HCP Mg. The uncertainties in DFT energies due to XC functionals is computed empirically, while the GF approach computes transport coefficients, and we quantify the probability distributions of transport predictions. Section 4.2 details the diffusion model of vacancy-mediated solute transport, and Section 4.3 lays out the methodology of uncertainty quantification. Section 4.4 explains the DFT parameters and XC functionals used to quantify the uncertainty in DFT parameters for input into the diffusion model. Section 4.5 discusses the distribution of diffusion coefficients and drag ratios of 61 solutes in Mg. We show that the GF approach enables the development of computationally efficient Bayesian sampling scheme. We show that the drag ratios distributions are highly non-normal, while diffusion coefficients follow log-normal distributions; we quantify the uncertainties in activation energies, and find these to be between 90 and 120 meV. We show that the experimentally measured solute diffusion coefficients in Mg fall within our quantified uncertainties for most solutes; the remaining outliers may either suggest different diffusion mechanisms than considered here, or possible issues with the experimental measurements.

4.2 Diffusion model

The Onsager coefficients $\underline{L}^{AB}$ are second rank tensors that relate the flux of species A to chemical potential gradients in species B [1]. For vacancy-mediated transport in a binary alloy, the fluxes $\mathbf{J}^{s}$ of solutes (s) and $\mathbf{J}^{v}$ of vacancies (v) are linearly related to (small) chemical potential gradients $\nabla\mu$,

$$
\begin{aligned}
\mathbf{J}^{s} &= -\underline{L}^{ss}\nabla\mu^{s} - \underline{L}^{sv}\nabla\mu^{v}, \\
\mathbf{J}^{v} &= -\underline{L}^{vs}\nabla\mu^{s} - \underline{L}^{vv}\nabla\mu^{v}.
\end{aligned}
\tag{4.1}
$$

The diagonal Onsager coefficients $\underline{L}^{ss}$ and $\underline{L}^{vv}$ quantify the solute and vacancy transport under their respective chemical potential gradients, which act as driving forces for diffusion. The off-diagonal Onsager coefficients $\underline{L}^{sv} = \underline{L}^{vs}$ quantify the "flux coupling" between solutes and vacancies: a driving force for vacancies also creates a flux of solutes, and vice versa. The solute diffusivity, from Fick's first law ($\mathbf{J}^{s} = -\underline{D}\nabla C_{s}$), in the dilute limit of solute concentration C_{s} is proportional to $\underline{L}^{ss}$

$$
\underline{D} = (k_{B}T / C_{s})\underline{L}^{ss}
\tag{4.2}
$$

where k_{B} is the Boltzmann constant and T is temperature [1]. The drag ratio, defined as $\underline{L}^{sv}(\underline{L}^{ss})^{-1}$, quantifies the drag of solutes via vacancies. A positive drag ratio implies

the flux of vacancies drags solutes in the same direction and a negative drag ratio implies the motion of solutes opposite to the flux of vacancies. The flux coupling between vacancies and solutes can lead to solute segregation to vacancy sinks such as grain boundaries and causes the Kirkendall effect [12].

A variety of methods are possible for computing diffusivities from atomistic details. These include stochastic methods like kinetic Monte Carlo [13−17], master-equation methods like the self-consistent mean-field method [18,19] and kinetic mean-field approximations [20−22], path probability methods for irreversible thermodynamics [23−25], GF methods [11,26−28], and Ritz variational methods [29−31]. A recent paper showed that many of these methods are, in fact, examples of a variational principle [32], which allows for the comparison of accuracy in connecting atomistic scale information to the mesoscale transport coefficients. That connection between atomistic scale information and transport coefficients can be most easily seen from the (modified) Einstein relation, where the Onsager tensor coefficients are the thermo-dynamic averages of mean-squared displacements of infinite time trajectories,

$$\underline{L}^{AB} = \lim_{t \to \infty} \left\langle \frac{(\mathbf{R}^A(t) - \mathbf{R}^A(0)) \otimes (\mathbf{R}^B(t) - \mathbf{R}^B(0))}{2t\Omega k_{\mathrm{B}} T} \right\rangle \tag{4.3}$$

where $\mathbf{R}^A(t) - \mathbf{R}^A(0)$ is the total displacement of all atoms of species A from time 0 up to time t, and Ω is the total volume of the sample. In the case of kinetic Monte Carlo, the trajectories are sampled directly from computed rates for a given atomic config-uration under the assumption of a Markovian process. The need for a finite length trajectory introduces a controlled approximation as longer trajectories reduce the error in transport coefficients. Other approaches, such as matrix methods, which produce the different "multifrequency" methods (8- and 13-frequency, for the case of HCP [33−35]) make particular uncontrolled approximations in the form of the rates, and for the computation of the infinite time limit. The recent GF approach [11] is exact in the dilute limit and avoids both approximations in the form of the rates and in the infinite time limit. All of these methods require accurate atomic-scale information about the transitions that cause diffusion in the crystal, and all assume Markovian processes for each discrete step in the trajectory.

Modeling vacancy-mediated solute diffusion requires the geometry of solute−vacancy complexes as shown in Fig. 4.1 and all possible vacancy jumps through these complexes as shown in Fig. 4.2. In the HCP crystal, there are two unique first nearest-neighbor vacancy−solute complexes: 1b, where a vacancy and a solute lie in the same basal plane, and 1p, where a vacancy and a solute lie in neighboring basal planes. There are seven more complex configurations—2p, 3c, 4p, 4b, 4b, 5p, and 6b—that are one transition away from 1b or 1p. Generally, the solute−vacancy binding energy for these seven configurations are ignored because they are significantly less than the 1b and 1p complexes, but such approximations can affect the transport coefficients if any of the seven configurations have significant binding energy. There are 15 symmetry unique transition states for vacancy jumps out of 1p and 1b complexes: two solute−vacancy exchange jumps, 1b-sol and 1p-sol, where a solute exchanges
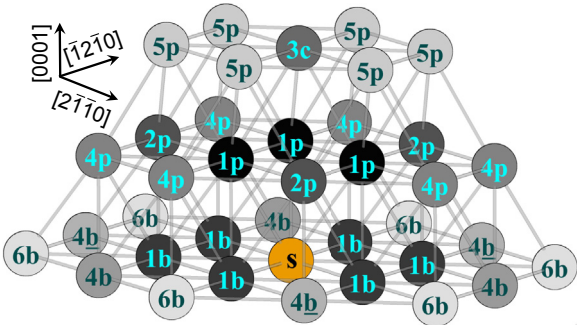
Figure 4.1 Possible vacancy−solute complexes out to sixth nearest neighbors in an HCP crystal. Complexes are identified by the position of the vacancy relative to the solute (orange "s"). Complexes are labeled by the shell distance between solute and vacancy (lighter colors correspond to larger separation), and with "b" (basal), "p" (prismatic), and "c" (c-axis). There are nine symmetrically unique complexes, with the vacancy in the 1b or 1p configurations closest to the solute.
From R. Agarwal, D.R. Trinkle, Exact model of vacancy-mediated solute transport in magnesium, Phys. Rev. Lett. 118 (2017) 105901.
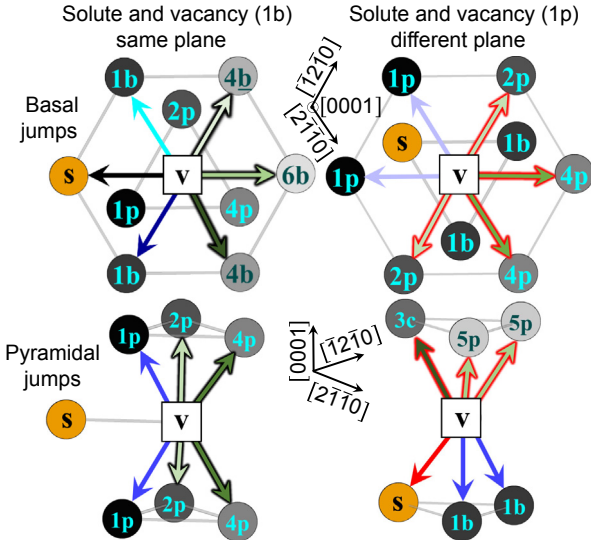

Figure 4.2 Vacancy (v) jumps in an HCP crystal from 1b and 1p complexes, divided into basal and pyramidal jumps. The 24 vacancy jumps consist of 15 symmetry unique transition states: two solute−vacancy exchanges (*black and red arrows*), four vacancy reorientations around the solute (*arrows in blue*), and nine solute−vacancy complex dissociations (*arrows in green with outline in black* from 1b configuration and *outline in red* from 1p configuration).
From R. Agarwal, D.R. Trinkle, Exact model of vacancy-mediated solute transport in magnesium, Phys. Rev. Lett. 118 (2017) 105901.

position with a vacancy; four reorientation jumps, 1b-1b, <u>1b-1b</u>, 1b-1p (or 1p-1b), and 1p-1p, where a vacancy moves around the solute and remains in the 1b or 1p complex; and nine dissociation jumps, 1b-4b, 1b-4b, 1b-6b, 1b-2p, 1b-4p, 1p-2p, 1p-4p, 1p-3c, and 1p-5p, where a vacancy jumps away from the interaction range of a solute. Note that the reverse of a dissociation jump is an association jump. The vacancy jump energy barriers between non−first neighbor solute−vacancy complexes are approximated with pyramidal ("pyr") or basal ("bas") vacancy jump energy barriers from the pure Mg crystal. This approximation will lead to errors if non−first neighbor solute−vacancy complexes have significant binding energies, and changes to the jump network barriers would need to be accommodated. Note that the vacancy jump network can be different for other elements with the same crystal structure; for example, unlike in Mg, the basal migration of vacancy passes through a metastable state in HCP-Ti [36,37] and HCP-Zr [38], which also requires proper treatment in vacancy-mediated solute transport.

The binding energy of solute−vacancy complexes, the vacancy jump network and rates between those complexes, and the equilibrium vacancy concentration are the inputs to our diffusion model. The uncertainties in these inputs get translated to the error bars on transport coefficients. The binding energy of a complex E_α^{bind} quantifies the interaction between a solute and a vacancy and is computed as

$$E_\alpha^{\text{bind}} = E[X + \text{sv}_\alpha] - E[X + \text{sv}_\infty], \tag{4.4}$$

where $E[X + \text{sv}_\alpha]$ is the energy of a system having host lattice of X, and one solute and one vacancy in configuration α and $E[X + \text{sv}_\infty]$ is the energy of a system where the distance between the solute atom and the vacancy approaches infinity. A positive or a negative value of binding energy denotes repulsive or attractive interaction between a solute and a vacancy, respectively. From harmonic transition state theory, the rate $\omega_{\alpha-\beta}$ for a vacancy to jump from complex α to β through the transition state $\alpha-\beta$ is

$$\omega_{\alpha-\beta} = \nu_{\alpha-\beta}^* \cdot \exp\left(-E_{\alpha-\beta}^{\text{mig}} / k_\text{B}T\right), \tag{4.5}$$

where $\nu_{\alpha-\beta}^*$ and $E_{\alpha-\beta}^{\text{mig}}$ are the attempt frequency and migration barrier for the vacancy transition, respectively. The migration barrier is computed using

$$E_{\alpha-\beta}^{\text{mig}} = E[X + \text{sv}_{\alpha-\beta}] - E[X + \text{sv}_\alpha], \tag{4.6}$$

where $E[X + \text{sv}_{\alpha-\beta}]$ is the energy of a system containing one solute and one vacancy at the transition state $\alpha - \beta$ in the host lattice of X. The attempt frequency is computed using the Vineyard expression [39] under the moving atom approximation [3,8], which is the product of three vibrational frequencies $\nu_{\alpha,p}$ associated with the moving atom at the initial state α divided by the product of two real vibrational frequencies $\nu_{\alpha-\beta,q}$ associated with the moving atom at the transition state

$$\nu^*_{\alpha-\beta} = \frac{\prod_{p=1}^{3} \nu_{\alpha,p}}{\prod_{q=1}^{2} \nu_{\alpha-\beta,q}}.$$ (4.7)

The equilibrium vacancy concentration in the solute-free system is

$$C_{\mathrm{v}} = \exp\left(-\frac{E_{\mathrm{v}}^{\mathrm{form}} - TS_{\mathrm{v}}^{\mathrm{form}}}{k_{\mathrm{B}}T}\right),$$ (4.8)

where $E_{\mathrm{v}}^{\mathrm{form}}$ and $S_{\mathrm{v}}^{\mathrm{form}}$ are the vacancy formation energy and entropy, respectively. The concentration $C_{\mathrm{v},\alpha}$ of solute−vacancy complex α is

$$C_{\mathrm{v},\alpha} = C_{\mathrm{v}}\exp\left(-\frac{E_{\alpha}^{\mathrm{bind}}}{k_{\mathrm{B}}T}\right)\exp\left(\frac{S_{\alpha}^{\mathrm{bind}}}{k_{\mathrm{B}}}\right)$$ (4.9)

where $E_{\alpha}^{\mathrm{bind}}$ and $S_{\alpha}^{\mathrm{bind}}$ are the solute−vacancy binding energy and binding entropy in complex α. The entropy $S_{\alpha}^{\mathrm{bind}}$ quantifies the change in atomic vibrations due to the formation of solute−vacancy complex α compared to when the solute and vacancy are infinitely far apart. Uncertainties may get introduced in solute−vacancy binding energies and entropies, vacancy migration barriers and their attempt frequencies, and vacancy formation energy and entropy due to the atomistic method used to compute them. For example, the DFT-computed quantities have uncontrolled error (c.f. Ref. [40]) due to the exchange-correlation treatment of electrons; as this error cannot be reduced by systematic improvement of computational parameters, we require quantification of the possible error.

An additional source of uncertainty in the computation of transport coefficients is the computational model itself, in particular, the treatment of correlated motion inherent in vacancy-mediated diffusivity. The state and transition state energies for different configurations can be easily transformed into equilibrium probabilities and rates, but the transformation of that data into transport coefficients is nontrivial. For an HCP material, there are the traditional 8- and 13-frequency models [33−35] that force approximations on both the form of the rates—imposing equality for cases that are not enforced by symmetry—and make uncontrolled approximations on the correlation coefficients. The correlation can be thought of as a correction to the "bare" diffusivity; in a kinetic Monte Carlo calculation, this is converged by taking increasingly long trajectories to compute the transport coefficients [32]. A recent GF-based method [11] analytically computes the transport coefficients for an infinitely dilute model of one solute and one vacancy; in this case, it is possible to mathematically compute the infinitely long trajectory limit. Moreover, this is significantly computationally efficient compared with, say, a kinetic Monte Carlo calculation and has the advantage of not introducing additional sources of uncertainty that an 8- or 13-frequency model might.

The GF approach is computationally more efficient, but it is worth understanding the computational effort as it motivates particular choices that we make in our uncertainty quantification approach. In order to compute the infinite trajectory limit for diffusion in the presence of a solute, we use the Dyson equation to compute it from the infinite trajectory limit *without* a solute. As the solute−vacancy interaction has a finite range, we can compute g, the vacancy GF with a solute, on a subspace of states with a nonzero solute−vacancy interaction, from the vacancy GF without a solute $g^{(0)}$ and the change in rates $\delta\omega$, as

$$g = \left(\left(g^{(0)} \right)^{-1} + \delta\omega \right)^{-1} \tag{4.10}$$

In addition, the size of the subspace to evaluate this matrix inverse is reduced by taking advantage of crystal symmetry; for the case shown in Fig. 4.1, this amounts to inverting a 17×17 matrix. However, in order to compute $g^{(0)}$, the GF calculation without a solute is evaluated for 42 different separation vectors; in our calculations, this takes the longest time in a particular calculation, due to the three-dimensional inverse Fourier transform (see Ref. [11] for specific details of the computational methodology used). Due to the computational cost, the implementation [41] caches values of $g^{(0)}$ that have been computed for a given set of rates; this is *independent* of the solute, and all of the solute-dependent effects enter through the $\delta\omega$ rate matrix. Normally, this is used to make the computation of multiple solutes at a single temperature more efficient; here, we will consider the sampling of the "pure vacancy" degrees of freedom separate from the solute degrees of freedom in order to increase the computational efficiency of the method. This is strictly a practical consideration which is not driven by an inherent need to separately treat the different degrees of freedom. However, as we will note below, the diffusivity of some solutes are more strongly affected by uncertainty in the vacancy data, while others are more strongly affected by uncertainty in the solute data, depending on which terms dominate in Eq. (4.10).

4.3   Methodology for uncertainty quantification

Computing uncertainties in solute transport coefficients require the probability distributions describing uncertainties in the inputs of diffusion model. We consider the uncertainties in the vacancy formation energy, solute−vacancy binding energies, and vacancy migration barriers. We assume that these energies θ follow a multivariate normal distribution $P(\theta)$

$$P(\theta) = \det(2\pi\Sigma)^{-1/2} \exp\left[-\frac{1}{2} \left(\theta - \overline{\theta} \right) \Sigma^{-1} \left(\theta - \overline{\theta} \right) \right], \tag{4.11}$$

where $\overline{\theta}$ is the vector of the mean, and Σ is a covariance matrix describing variance and correlations between the different energies. In case of HCP Mg, the energy vector

θ is $\left[E_v^{\text{form}}, E_{\text{pyr}}^{\text{mig}}, E_{\text{bas}}^{\text{mig}}, E_{1p}^{\text{bind}}, E_{1b}^{\text{bind}}, E_{1p-\text{sol}}^{\text{mig}}, E_{1b-\text{sol}}^{\text{mig}}, E_{1p-1p}^{\text{mig}}, E_{1p-1b}^{\text{mig}}, E_{1b-1b}^{\text{mig}}, E_{1b-1b}^{\text{mig}}, \right.$

$\left. E_{1p-2p}^{\text{mig}}, E_{1p-3c}^{\text{mig}}, E_{1p-4p}^{\text{mig}}, E_{1p-5p}^{\text{mig}}, E_{1b-2p}^{\text{mig}}, E_{1b-4p}^{\text{mig}}, E_{1b-4b}^{\text{mig}}, E_{1b-4b}^{\text{mig}}, E_{1b-6b}^{\text{mig}} \right]^{\text{T}}$, where the
first three elements are solute-independent energies (vacancy formation, and vacancy
migration barrier in pyramidal and basal direction of bulk Mg). The remaining 17
elements of θ are solute-dependent energies consisting of solute−vacancy binding at
1p and 1b complex, and 15 vacancy migration barriers near the solute. For simplicity,
we assume no uncertainties in the vacancy formation entropy, solute−vacancy binding
entropies, and the attempt frequency of vacancy migrations. For mass transport, the
attempt frequencies for atomic jumps in materials typically are dominated by the mass
of the chemical species involved (which we account for in our "jumping atom"
approach). It would be extremely unusual for different exchange-correlation potentials
to predict variations even as large as a factor of two for a given solute, as that would
indicate changes in atomic force constants on the order of a factor of four.

   We separate the distribution of energies into solute-independent (v) and solute-
dependent (s) energies for computational efficiency. The energy vector θ in separated
form is

$$\theta = \begin{pmatrix} \theta^{\text{v}} \\ \theta^{\text{s}} \end{pmatrix}, \tag{4.12}$$

and the covariance matrix in a block diagonal is

$$\Sigma = \begin{pmatrix} \Sigma^{\text{vv}} & \Sigma^{\text{vs}} \\ \Sigma^{\text{sv}} & \Sigma^{\text{ss}} \end{pmatrix}. \tag{4.13}$$

   We rewrite the probability distribution of solute−vacancy energies as

$$P(\theta) = P^{\text{v}}(\theta^{\text{v}}) P^{\text{s}}(\theta^{\text{s}}|\theta^{\text{v}}), \tag{4.14}$$

where $P^{\text{v}}(\theta^{\text{v}})$ is the multivariate normal distribution of solute-independent energies
with covariance matrix Σ^{vv} and mean $\overline{\theta}^{\text{v}}$, and $P^{\text{s}}(\theta^{\text{s}}|\theta^{\text{v}})$ is the distribution of solute-
dependent energies for a given θ^{v} of solute-independent energies. The distribution
$P^{\text{s}}(\theta^{\text{s}}|\theta^{\text{v}})$ is a multivariate normal distribution with covariance matrix $\Sigma^{\text{ss}} - \Sigma^{\text{sv}}(\Sigma^{\text{vv}})^{-1}\Sigma^{\text{vs}}$ and mean $\overline{\theta}^{\text{s}} + \Sigma^{\text{sv}}(\Sigma^{\text{vv}})^{-1}(\theta^{\text{v}} - \overline{\theta}^{\text{v}})$. Note that the latter covariance
matrix is independent of θ^{v} or $\overline{\theta}^{\text{v}}$, so it needs to be computed once unlike the mean
which is different for every solute-independent energy vector. This separation of
solute−vacancy energies has two advantages: (1) sampling of solute-independent
energies remains the same for all the solutes, so only needs to be performed
once. (2) The GF approach requires computation of the vacancy GF $g^{(0)}$ which is
computationally expensive and depends only on the solute-independent energies; this
quantity can be computed once and saved to use in later calculations.

A Bayesian framework is employed to determine the uncertainties in solute transport coefficients. The average of a function $f(\theta^{\mathrm{v}}, \theta^{\mathrm{s}}; T)$ at temperature T is

$$\langle f(\theta^{\mathrm{v}}, \theta^{\mathrm{s}}; T) \rangle = \int_{\theta^{\mathrm{v}}} d\theta^{\mathrm{v}} P^{\mathrm{v}}(\theta^{\mathrm{v}}) \left[\int_{\theta^{\mathrm{s}}} d\theta^{\mathrm{s}} P^{\mathrm{s}}(\theta^{\mathrm{s}}|\theta^{\mathrm{v}}) f(\theta^{\mathrm{v}}, \theta^{\mathrm{s}}; T) \right]. \tag{4.15}$$

Generally, the θ^{v} vector has smaller dimension (three for HCP Mg) compared to the θ^{s} vector (17 for HCP Mg); this can make Gauss−Hermite (GH) quadrature a computationally efficient scheme for the integration over θ^{v} domain. Due to the large dimension of θ^{s}, the integration over the θ^{s} domain is performed stochastically using multivariate distribution sampling of $P^{\mathrm{s}}(\theta^{\mathrm{s}}|\theta^{\mathrm{v}})$. Then, the numeric approximation to the average of a function $f(\theta^{\mathrm{v}}, \theta^{\mathrm{s}}; T)$ at temperature T is

$$\langle f(\theta^{\mathrm{v}}, \theta^{\mathrm{s}}; T) \rangle \approx \sum_{i=1}^{N_{\mathrm{GH}}} \frac{w_i}{N} \sum_{j=1}^{N} f\left(\theta^{\mathrm{v},i}, \theta^{\mathrm{s},j}, T\right), \tag{4.16}$$

where N_{GH} and N are the number of GH quadrature points and stochastic multivariate samples, respectively. The $\theta^{\mathrm{v},i}$ are the GH quadrature points with weights w_i and $\theta^{\mathrm{s},j}$ are the multivariate samples for a given $\theta^{\mathrm{v},i}$, obtained by sampling $P^{\mathrm{s}}(\theta^{\mathrm{s}}|\theta^{\mathrm{v}})$. The covariance matrices for the θ^{v} parameters are computed empirically from a set of different exchange-correlation potentials (c.f. Section 4.4). The covariance matrices for the θ^{s} parameters are computed empirically from a set of different exchange-correlation potentials *and* evaluated over a set of 13 selected solutes under the assumption that the covariance in the solute parameters is *independent* of the solute chemistry; this assumption was found to be valid for the 13 selected solutes but is applied to a total set of 61.

In what follows, we evaluate uncertainties for two mass transport predictions: the diffusivity, D, and the drag ratio $\underline{L}^{\mathrm{sv}}/\underline{L}^{\mathrm{ss}}$, which require different uses of averages and distributions from Eq. (4.16). In the case of diffusivity, we find that the diffusivities are log-normally distributed for our specific case of solute diffusion in Mg. While the uncertainty in the diffusivity is important, we are also interested in the propagation of uncertainties to the Arrhenius *parameters* that represent the temperature dependence; we explain our approach below. The drag ratios, on the other hand, are found to be highly non-normal. To describe the uncertainties in the drag ratios, we compute empirical probability distributions and compute medians and upper and lower quartiles as a function of temperature for all solutes, along with skewness for a set of solutes to highlight the non-normality of the distributions. This is expanded further in Section 4.5.3.

A correlated error fit on diffusion coefficients with respect to temperature is essential to obtain uncertainties in Arrhenius parameters. For the diffusivities, $\underline{D} = k_{\mathrm{B}} T \underline{L}^{\mathrm{ss}} / C_{\mathrm{s}}$ (c.f. Eq. 4.2), we find that they follow log-normal distributions; however, the values at each temperature T are highly correlated with each other. Typically, one reports the activation barrier and prefactor for diffusivity following the Arrhenius form,

$$\log_{10}D(T) = \log_{10}D_0 - \left(\frac{Q \cdot \log_{10}e}{k_{\mathrm{B}}}\right)\frac{1}{T}, \tag{4.17}$$

where the Arrhenius parameters $\log_{10}D_0$ and Q denote the logarithm of the diffusion prefactor and the activation energy for diffusion, respectively. To propagate (highly correlated) uncertainty from the $D(T)$ data to uncertainty in the parameters Q and D_0, we consider the determination of the parameters from the system of linear equations,

$$\begin{pmatrix} \log_{10}D(T_1) \\ \vdots \\ \log_{10}D(T_m) \end{pmatrix} = \begin{pmatrix} 1 & -\dfrac{\log_{10}e}{k_{\mathrm{B}}T_1} \\ \vdots & \vdots \\ 1 & -\dfrac{\log_{10}e}{k_{\mathrm{B}}T_m} \end{pmatrix} \begin{pmatrix} \log_{10}D_0 \\ \\ Q \end{pmatrix}, \tag{4.18}$$

$$F = AX,$$

where F is an m dimensional vector of the logarithm of diffusion coefficients at distinct temperatures, A is the Vandermonde matrix of size $m \times 2$, and X is the two-dimensional vector of Arrhenius fitting parameters. Under the assumption that $\log_{10}D(T)$ follows a multivariate normal distribution for different temperatures, the covariance matrix of Arrhenius parameters Σ^X of size 2×2 is

$$\Sigma^X = \left(A^{\mathrm{T}}A\right)^{-1}A^{\mathrm{T}}\Sigma^F A\left(A^{\mathrm{T}}A\right)^{-1}, \tag{4.19}$$

where Σ^F is the covariance matrix of $\log_{10}D(T)$ of size $m \times m$. In our case, where we find log-normally distributed diffusivities, we can use an analytic approximation based on the Jacobian matrix; $\log_{10}D(T)$ can be approximated as

$$\log_{10}D(\theta, T) \approx \log_{10}D(\overline{\theta}, T) + J \cdot (\theta - \overline{\theta}), \tag{4.20}$$

where J is the Jacobian matrix evaluated at $\overline{\theta}$, whose J_{ij} element is the partial derivative of $\log_{10}D(\theta, T_i)$ at temperature T_i with respect to the jth component of the θ vector: $\frac{\partial \log_{10}D(\theta, T_i)}{\partial \theta_j}\big|_{\theta=\overline{\theta}}$. The analytical covariance matrix of F is then

$$\Sigma^F = J \, \Sigma \, J^{\mathrm{T}}, \tag{4.21}$$

where Σ is the previously defined covariance matrix of solute−vacancy energies.

4.4 Computational details

DFT calculations compute the solute−vacancy energy vector θ using the Vienna ab-initio simulation package VASP 5.4.4 [42]. The VASP software package performs electronic structure calculations based on plane-wave basis sets. We use the projector-augmented wave pseudopotentials [43] generated by Kresse [44] to describe the core electrons of 13 solutes and Mg atoms; the valence configurations are the same as used in the previous study [5] and summarized in Table 4.1. We use a $4\times 4\times 3$ Mg supercell containing 96 atoms with a $6 \times 6 \times 6$ gamma−centered Monkhorst−Pack k-point mesh for Ag, Al, Hf, Li, Mn, Sb, Sc, Sn, Ti, and Zn, while Ca, Ce, and La require a $5 \times 5 \times 3$ Mg supercell containing 150 atoms with a $5 \times 5 \times 6$ k-point mesh due to large vacancy relaxations near the solutes in 1p and 1b complexes. Methfessel−Paxton smearing [45] with an energy width of 0.25 eV is sufficient to integrate the density of states. We use the energy convergence tolerance of 10^{-8} eV for the electronic self-consistency cycle. We use a plane-wave energy cutoff of 500 eV which is sufficient to give an energy convergence of less than 1 meV/atom. All the atoms are relaxed using a conjugate gradient method until the force on each atom is less than 5 meV/Å. The climbing-image nudged elastic band [46] method with one intermediate image determines the transition state configurations and energies.

We perform DFT calculations with different exchange-correlation (XC) functionals using an efficient scheme to compute the covariance matrix of energies. We treat electron exchange and correlation for pure Mg using five different functionals—the local density approximation (LDA) [47], the generalized gradient approximations (GGA) by Perdew, Burke, and Ernzerhof (PBE) [48], Perdew−Wang-91 (PW91) [49], and PBE for solids (PBEsol) [50], and a strongly constrained and appropriately normed (SCAN) meta-GGA [51]. Table 4.2 lists the lattice parameters, vacancy formation energy, and vacancy migration barriers of bulk Mg for these five XC functionals. This table is used to compute the covariance in vacancy formation energy and vacancy migration barriers in bulk Mg due to XC functionals. We use PBE, LDA, and SCAN XC functional for 13 solutes (listed in previous paragraph and Table 4.1) to

Table 4.1 Electronic configurations for PAW pseudopotentials used for Mg and the 13 solutes that quantified the covariances in solute parameters.

Element	Valence	Element	Valence
Mg	$3s^2 3p^0$	Li	$2s^1 2p^0$
Ag	$5s^1 4d^{10}$	Mn	$3p^6 4s^2 3d^5$
Al	$3s^2 3p^1$	Sb	$5s^2 5p^3$
Ca	$3s^2 3p^6 4s^2$	Sc	$3p^6 4s^2 3d^1$
Ce	$6s^2 5d^1 4f^1$	Sn	$5s^2 5p^2$
Hf	$5p^6 6s^2 5d^2$	Ti	$3p^6 4s^2 3d^2$
La	$4d^{10} 4f^1$	Zn	$3d^{10} 4p^2$

Table 4.2 Prediction of the lattice parameters a and c, vacancy formation energy $E_{\mathrm{v}}^{\mathrm{form}}$, and vacancy migration barriers in the pyramidal $E_{\mathrm{pyr}}^{\mathrm{mig}}$ and basal $E_{\mathrm{bas}}^{\mathrm{mig}}$ directions for bulk HCP Mg using five XC functionals.

Property	LDA	PBE	PBEsol	PW91	SCAN	Experiments
a (Å)	3.13	3.19	3.17	3.19	3.17	3.19 [52]
c (Å)	5.09	5.19	5.16	5.19	5.16	5.17 [52]
$E_{\mathrm{v}}^{\mathrm{form}}$ (eV)	0.85	0.81	0.87	0.76	0.95	0.58 [53], 0.79 [54], 0.81 [55]
$E_{\mathrm{pyr}}^{\mathrm{mig}}$ (eV)	0.43	0.42	0.43	0.40	0.49	0.45 [56], 0.59 [57]
$E_{\mathrm{bas}}^{\mathrm{mig}}$ (eV)	0.41	0.40	0.41	0.38	0.48	0.45 [56], 0.57 [57]

The DFT predictions of lattice parameters are similar within a 0.07 Å range, while $E_{\mathrm{v}}^{\mathrm{form}}$ varies by 190 meV and the migration barriers vary by 100 meV. The last column lists the experimental measurements.

compute the covariance in solute-dependent energies. We make use of fully atomically relaxed supercells obtained using the PBE functional as a starting guess for the DFT calculations employing LDA and SCAN functional for computational efficiency. We also scale the PBE obtained geometries with the bulk Mg lattice parameters (a and c) corresponding to LDA or SCAN and compute the energy and the atomics forces of the scaled supercell. Instead of relaxing the atomic positions in the scaled supercell, we approximate the relaxation energy (E_{relax}) using

$$E_{\mathrm{relax}} = -\frac{1}{2}F_{\mathrm{atomic}}\mathrm{GF}_{\mathrm{atomic}}^{T}, \tag{4.22}$$

where G is the harmonic lattice GF of the supercell (the pseudoinverse of the force constant matrix of bulk Mg from PBE) and F_{atomic} is the atomic force vector computed from LDA or SCAN. So, the DFT energy using this approximate scheme is the sum of first ionic step energy and the relaxation energy computed using Eq. (4.22). We find an energy difference of less than 5 meV between our approximate and a fully relaxed calculation for Ag using SCAN functional for binding energies of 1p and 1b, and migration barriers of 1p-sol and 1b-sol. Our efficient scheme reduces the computational effort of 10 ionic steps on an average compared to regular DFT relaxation with a negligible sacrifice in accuracy. We use the above scheme to obtain binding energies and migration barriers for 13 solutes with three different exchange-correlation potentials in order to quantify the covariances of solute parameters.

4.5   Results and discussion

4.5.1   Distribution of parameters

We assume that the energies predicted by different XC functionals would obey a normal distribution and Fig. 4.3 shows the variance and the correlations in solute−vacancy energies computed using different sets of XC functionals. Solute transport
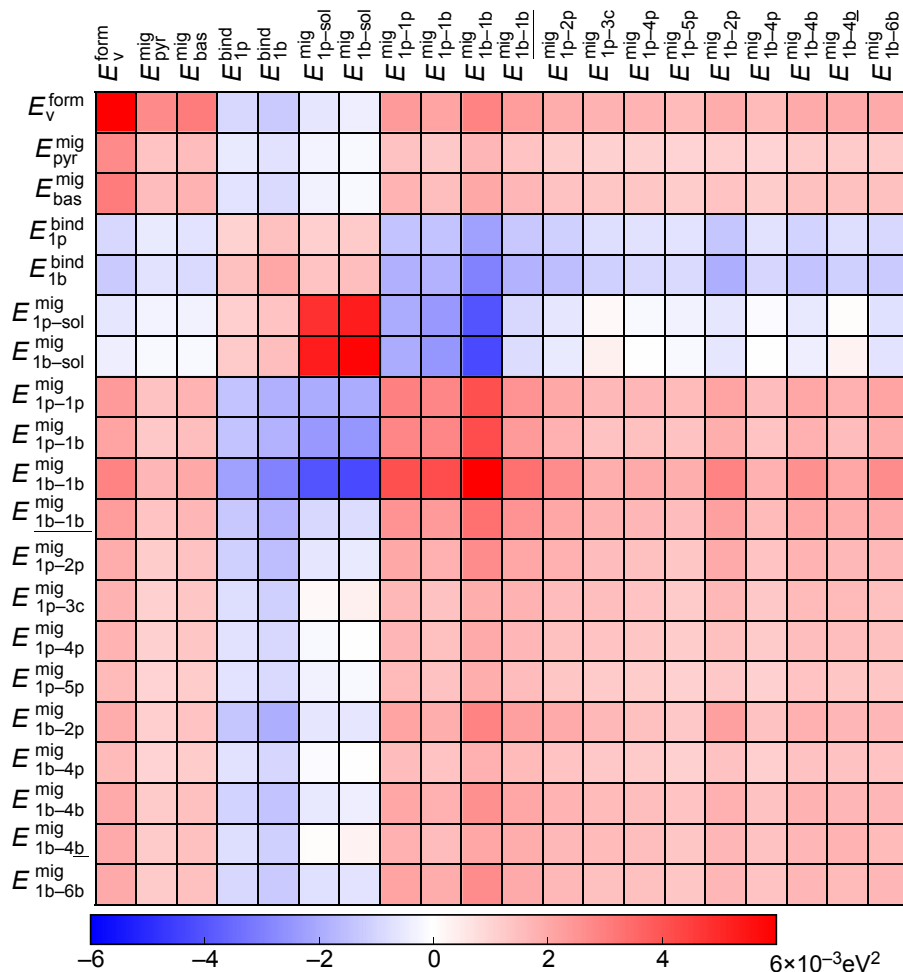
Figure 4.3 Covariance matrix of energies for 20 configurations in Mg. There are 3 solute-independent energies—vacancy formation energy and vacancy migration barriers in the pyramidal and basal directions in bulk Mg—and 17 solute-dependent energies—2 solute−vacancy binding energies and 15 vacancy migration barriers in the presence of a solute. The DFT data using three XC functionals (PBE, SCAN, and LDA) for 13 solutes is used to compute the covariance matrix. The vacancy formation energy, the solute−vacancy exchange barriers, and the 1b-1b vacancy reorientation barrier show the largest variance with values between 0.005 and 0.006 eV^2. Refer to Figs. 4.1 and 4.2 for the geometries of these 20 configurations.

in Mg is determined by 20 energies consisting of 3 solute-independent energies and 17 solute-dependent energies. The solute-independent part of the covariance matrix is computed using the energies obtained from five XC functional for bulk Mg. The solute-dependent part of the covariance matrix is computed using the DFT energies for 13 solutes and employing three XC functionals as mentioned in Section 4.4.

To compute the covariances in the solute−vacancy interactions, we assume that the variations are *independent* of the particular solute being considered, so that our 13 solutes and 3 XC functionals are essentially random inputs. However, as each solute has its own solute−vacancy interaction, we subtract the PBE functional values from the SCAN and LDA values to compute the covariances, which reduce the number of effective degrees of freedom. The (i, j) entry of the covariance matrix Σ is

$$\Sigma_{ij} = \frac{1}{M-1} \left[\sum_{p=1}^{M} \theta_i^p \theta_j^p - \sum_{p=1}^{M} \theta_i^p \sum_{p=1}^{M} \theta_j^p \right], \tag{4.23}$$

where θ_i^p is the energy of the ith configuration (refer to Figs. 4.1 and 4.2 for the geometries of these 20 configurations) in the pth energy vector and M is the number of energy vectors. The vacancy formation energy, the solute−vacancy exchange barriers, and the 1b-1b vacancy reorientation barrier show the largest standard deviation of $\approx$ 70 meV, while the standard deviations in the energies of the other configurations lie between 10 and 50 meV. Note that we have computed our covariances using the distributions from 13 solutes; we now use the *mean values* for each solute from our previous study [5,58] and combine with these covariances to model uncertainties for 61 different solutes.

4.5.2   Distribution of diffusivities

Fig. 4.4 shows that the logarithm of diffusion coefficients ($\log_{10} D$) at different temperatures follows a normal distribution and different sampling parameters are required to converge to this distribution for all the solutes. We use Eq. (4.14) to separate the sampling of solute-dependent and solute-independent energies and use Eq. (4.16) to generate the distributions of $\log_{10} D$. Multinormal GH quadrature [59] integrates over the vacancy formation energy, and the vacancy migration barriers in pyramidal and basal directions in bulk Mg, while multivariate normal sampling integrates over the 17 solute-dependent energies. We find that faster solutes require a larger number of GH points (finer grids) i.e., 2500, 1600, 900, 400, and 100 for Ca, Li, Sn, Al, and Os, respectively, to converge diffusivities to log-normal distributions, otherwise coarser GH grids lead to multimodal distributions. Slower solutes are dependent on solute−vacancy exchange barriers requiring a large number of multivariate samples to integrate over solute-dependent energies; we use 50,000, 50,000, 10,000, 2500, and 1000 samples for Os, Al, Sn, Li, and Ca, respectively. We verify the normality of $\log_{10} D$ at different temperatures by computing the skewness, kurtosis, and the quantile−quantile plots of the distributions. The standard deviation of the $\log_{10} D$ distribution decreases with increasing temperature as thermal energy $k_B T$ reduces the effect of uncertainties in solute−vacancy energies. It should be noted that the normality of the distribution of the logarithm of the diffusion coefficients follows from the multivariate normal distribution of the uncertainty in parameters, and the domination of particular jumps in the diffusion network.
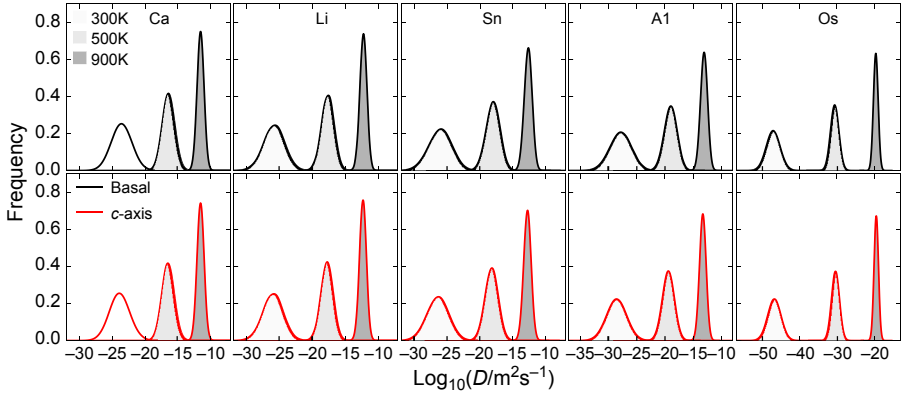
Figure 4.4 Distributions of the logarithm of diffusion coefficients $\log_{10}(D/\text{m}^2\text{s}^{-1})$ at 300K (light gray), 500K (gray), and 900K (dark gray) for Ca, Li, Sn, Al, and Os in Mg in the basal plane (black) and along the c-axis (red). The diffusion coefficients follow log-normal distributions and the widths decrease with temperature. The mean diffusivities of these five solutes are in the order $D_{\text{Ca}} > D_{\text{Li}} > D_{\text{Sn}} \approx D_{\text{Mg}} > D_{\text{Al}} > D_{\text{Os}}$ with respect to self-diffusion coefficient of Mg D_{Mg}. Faster solutes require a larger number of Gauss–Hermite quadrature points for solute-independent vacancy energetics and fewer multivariate samples for solute-dependent vacancy energetics compared to slower diffusing solutes to converge diffusivities to log-normal distributions.

The logarithm of diffusion coefficients obeys a multivariate normal distribution with respect to temperatures and we compute the covariance matrices of this distribution using stochastic sampling and an analytical method as discussed in Section 4.3. In the previous paragraph, we showed that our sampling scheme produces a normal distribution for $\log_{10}D$ at different temperatures. We also find that $\log_{10}D$ is positively correlated—Pearson correlation coefficient close to one—at different temperatures and obeys a multivariate normal distribution. We compute the covariance matrix of this multivariate distribution at eight temperatures between 300−923K using stochastic sampling and analytically using Eq. (4.21). The maximum relative difference for an entry in the covariance matrices between both of these methods is less than 5% for Ca, Li, Al, Sn, and Os. The analytical method is more computationally efficient than the sampling method because it only requires 40 diffusion calculations to compute the Jacobian for Eq. (4.21) using finite differences while sampling requires diffusion calculations for every stochastic sample. Since we find good agreement of covariance matrices between both the methods, we use the efficient analytical method to study uncertainties in the diffusion coefficients of 61 solutes.

We perform correlated error fits of solute diffusion coefficients with temperature using Eqs. (4.17)−(4.19) to compute the covariance matrix of Arrhenius parameters (Q and $\log_{10}D_0$). Fig. 4.5 shows that the standard deviation of the activation energy for diffusion lies between 90 and 115 meV for 61 solutes. The solute−vacancy exchange jumps 1b-sol and 1p-sol control the diffusion of solutes in the basal plane and along the c-axis for Ga, Ge, As, and the d-block solutes except Y and La [5]. Since the uncertainties in exchange barriers are the same for all the solutes (refer to Fig. 4.3),
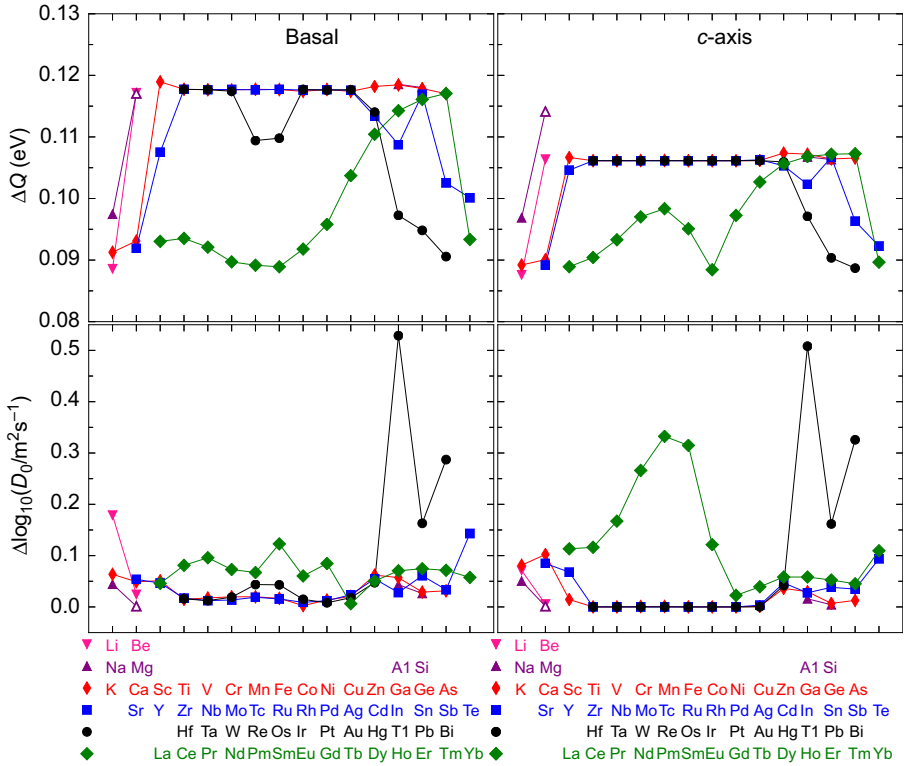
Figure 4.5 Uncertainties in the activation energy of diffusion ΔQ (top row) and the log of the diffusivity prefactor $\Delta \log_{10}(D_0/\mathrm{m^2 s^{-1}})$ (bottom row) in the basal plane and along the c-axis for 61 solutes in Mg. The activation energy uncertainties lies in a narrow interval of $90-120$ meV for all the solutes, and the uncertainties in the diffusion prefactor are very small since the attempt frequencies are kept constant in our analysis. The solutes Tl, Pb, Bi, Li, Te, and the first half of the lanthanides have more than one vacancy transition rate dominating in the temperature interval of $300-923$K, which gives rise to larger values of $\Delta \log_{10} D_0$.

the aforementioned 31 solutes show a similar standard deviation of 115 meV in the activation energy. In contrast, the diffusion of s-block solutes, lanthanides, Y, In, Sn, Sb, Te, Tl, Pb, and Bi depends on the vacancy exchanges with Mg atoms happening near the solute [5]. Since there are multiple types of vacancy exchanges with Mg atoms, the standard deviation of activation energy for these solutes varies between 90 and 115 meV. The standard deviation of the diffusion prefactor $\log_{10} D_0$ is negligible because the attempt frequencies of vacancy jumps are kept constant. In contrast, the s-block solutes, lanthanides, Y, In, Sn, Sb, Te, Tl, Pb, and Bi, show a nonzero standard deviation for $\log_{10} D_0$ due to competing vacancy rates across the fitting range of $300-923$K.

Fig. 4.6 shows the computed solute diffusion coefficients against available experimental measurements. The solute−vacancy energetics obtained using the PBE XC functional informs the GF approach [11] to compute mean diffusion coefficient [5].
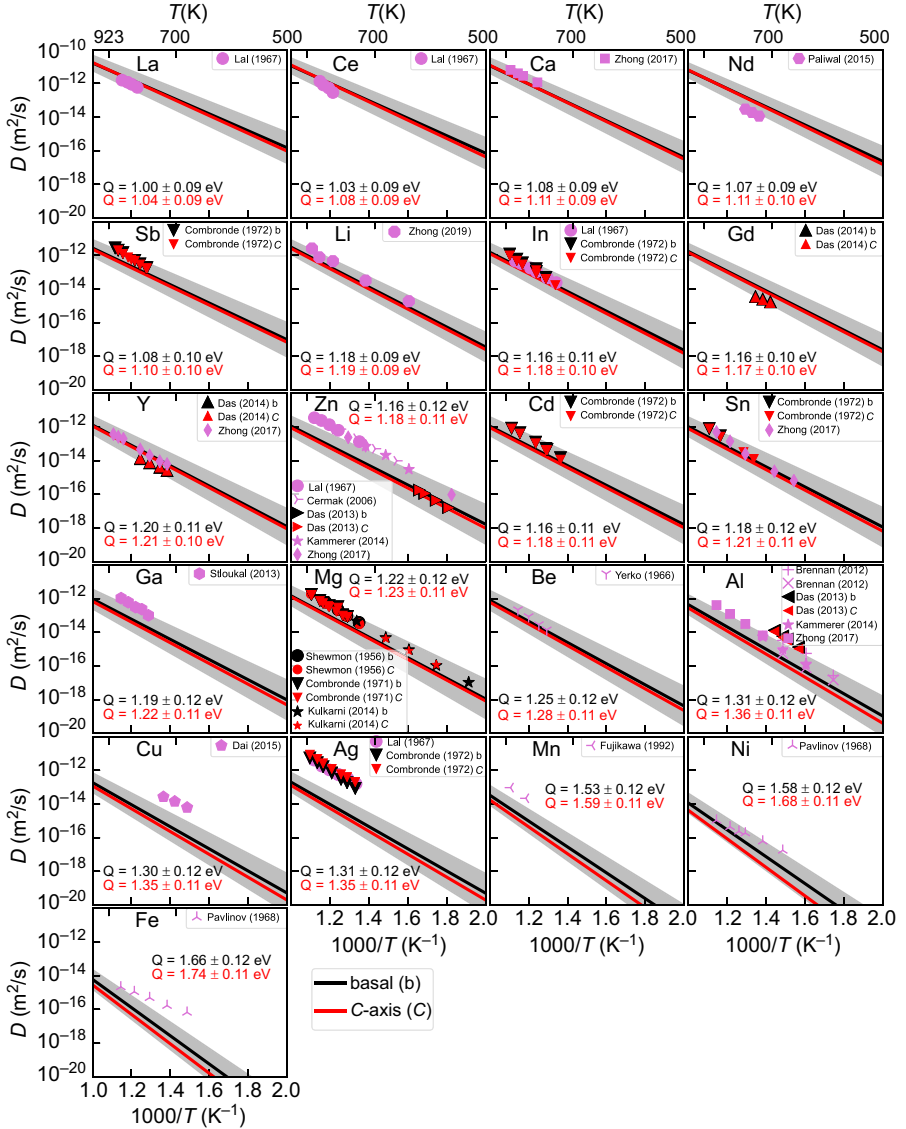
Figure 4.6 Solute diffusion coefficients D along with their error bars computed using the GF approach compared with the available experimental data. We arrange the Arrhenius plots of 20 solutes and Mg self-diffusion in decreasing order of computed diffusivity. Solid lines represent diffusion coefficients computed using the GF approach and symbols represent experimental measurements. Black and red denote diffusion in the basal(b) plane and along the c-axis, while pink symbols are the average diffusion coefficients from experimental polycrystalline measurements. The upper and lower bounds of the gray regions give the standard deviation of diffusion coefficients in the basal plane. We omit the uncertainties in diffusion coefficients along the c-axis since they are similar to the basal plane. We annotate the activation energies Q of diffusion along with their standard deviation in both directions. The experimentally measured diffusion coefficients fall within the computed error bars for all the solutes except Cu, Ag, Mn, and Fe.

The standard deviation of Arrhenius parameters shown in the last paragraph coupled with the mean diffusion coefficients is compared with the available experimental measurements [60−78]. The diffusion coefficient predictions are well within the computed error bars compared to the experimental measurements for 13 of the 17 solutes—La, Ce, Ca, Nd, Sb, Li, In, Gd, Y, Zn, Cd, Sn, Ga, Mg, Be, Al, and Ni. The disagreements for Cu, Ag, Mn, and Fe may suggest a diffusion mechanism other than vacancy mediated such as an interstitial mechanism or a combination of interstitial and vacancy mechanisms, since the experimental diffusion coefficients are larger than the theoretical predictions.

4.5.3 Distribution of drag ratios

Fig. 4.7 shows that the drag ratio distributions are not normal and have long tails on either side of the median. We use 36 GH points and 50,000 multivariate samples to obtain the drag ratio distribution in the temperature range of 300−923K for W, Li, Ca, Gd, and Zr. Drag ratios are positive due to the vacancy reorientations around the solute via inner or outer ring networks in HCP Mg [5]. The solutes W and Li have positive drag ratios due to faster vacancy reorientation rates in the inner ring networks, while Ca and Gd have positive drag ratios due to faster vacancy reorientation rates in the outer ring networks. The repulsive interaction between a vacancy and a Zr atom makes escape rates faster than the reorientation rates which lead to no drag. In case of W and to a lesser extent for Ca at 300K, the distribution is strongly peaked near one, which may be due to the insensitivity of vacancy reorientation around the solute to variations of 50−75 meV in solute−vacancy energies. The distribution for W, Ca, and Li spread out with temperature, while they narrow for Gd and Zr.

The skewness of the drag ratio distributions quantifies the nature of the tails and highlights the deviation from a normal distribution, as shown in Fig. 4.8. The drag ratio
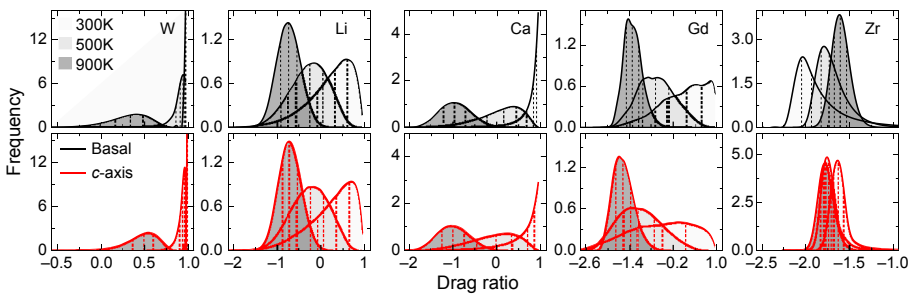

Figure 4.7 Distributions of the drag ratio at 300K (light gray), 500K (gray), and 900K (dark gray) for W, Li, Ca, Gd, and Zr in Mg in the basal plane (black) and along the *c*-axis (red). The three dashed vertical lines at each temperature represent lower quartiles, median, and upper quartiles of the drag ratio distribution. The drag ratio has a maximum value of one; hence, the distributions are not normal distributions. The drag ratio distributions for W and Ca at 300K are strongly peaked near one, while Li, Gd, and Zr have a spread in the distribution at 300K. Fig. 4.8 quantifies the tails of the drag ratio distributions based on skewness.
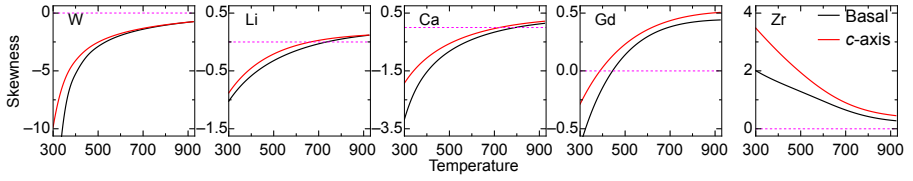
Figure 4.8 Skewness of the drag ratio distributions for W, Li, Ca, Gd, and Zr in Mg in the basal plane (black) and along the *c*-axis (red). A negative skewness indicates a longer tail on the left side compared to the right side of the distribution and vice versa. The drag ratio distributions remain negatively and positively skewed for W and Zr, respectively, in the temperature range of 300−923K. The skewness for Li, Ca, and Gd changes sign from negative to positive with temperature, i.e., the distribution of these three solutes is left-tailed at 300K, while right-tailed at 900K (c.f. Fig. 4.7).

distributions of W and Zr have long left and right tails in the temperature range of 300−923K, respectively, but the distribution becomes symmetric as temperature increases. In case of Li, Ca, and Gd, the distribution is left-tailed at lower temperatures and becomes right-tailed at higher temperatures.

Figs. 4.9−4.11 show the three quartiles of the drag ratio distributions for 61 solutes and we find that drag ratio is sensitive to the uncertainties in solute−vacancy energies with maximum uncertainty near the crossover temperature. We generate the drag ratio distributions using stochastic sampling in the temperature range of 300−923K. Figs. 4.9 and 4.10 show the drag distribution for solutes whose positive drag ratio is due to inner ring and outer ring networks, respectively, while Fig. 4.11 shows the solutes whose highly repulsive binding with the vacancy leads to no drag. The IQR—difference between the upper and lower quartiles—quantifies the spread of drag distributions. The drag ratio distribution is highly peaked at one (i.e., IQR of zero) near 300K for all the solutes in Fig. 4.9 except Al, Cr, V, Cd, and Li and for Sr, K, Te, Eu, La, and Sb in Fig. 4.10. We observe that IQR increases with temperature, achieving a maximum value near the median crossover temperature (where the drag ratio becomes zero) and then decreases with temperature for all solutes whose median of drag ratio distribution show a crossover. Note that the IQR maximas are flat and changes by only 0.01 within 100K temperature interval around the maxima. The maximum uncertainty in drag ratio near crossover may be because the variation in solute−vacancy energies changes the dominant mechanism since the mechanism for drag—vacancy motion around the solute through ring networks—and mechanism against drag—vacancy escape from the solute interaction range—cancels out at crossover. It is worth noting that the statistics we extract for each temperature describe the distribution of predictions for a given temperature, but there will be correlations between the predictions of drag ratios at different temperatures. This is similar to the correlation between predictions of diffusivity at different temperatures that we noted in Section 4.5.2. Given the non-normality of the distributions of drag ratios at each temperature, the best approach to quantifying the correlations across different temperatures would be empirical methods, like stochastic collocation [79].
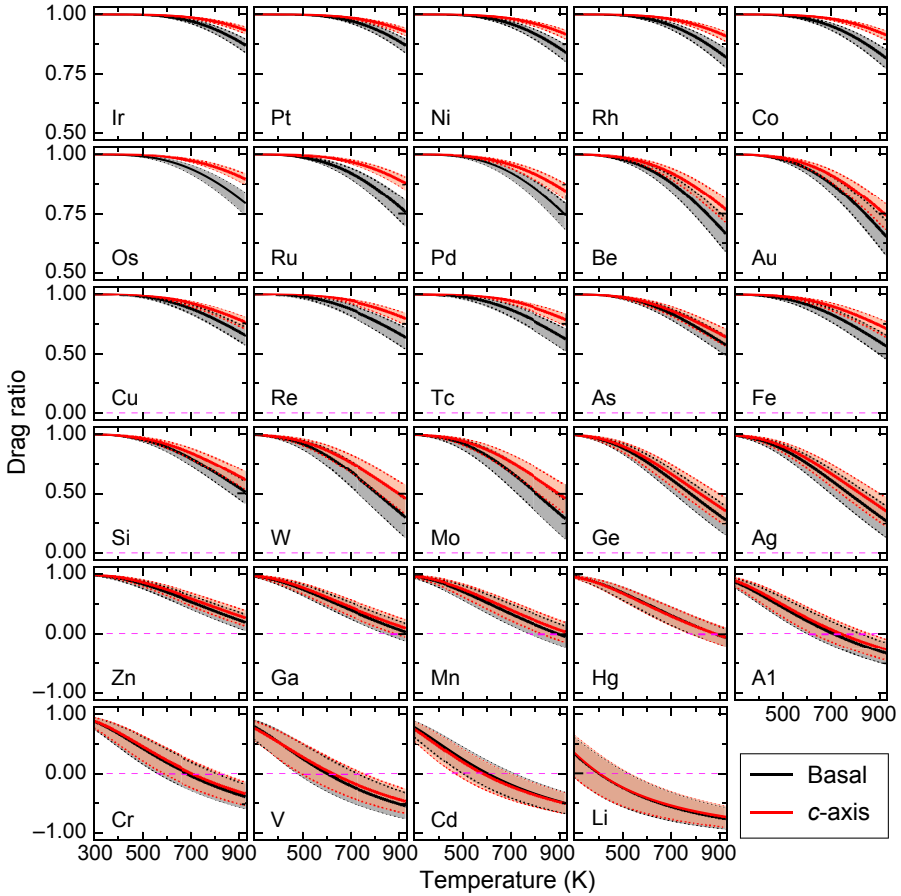
Figure 4.9 Three quartiles of the drag ratio distributions in the basal plane (black) and along the
c-axis (red) for solutes where inner ring networks lead to reorientation of the vacancy around
the solute. Solid lines represent the median of the drag ratio distributions and the dotted lines
representing the upper and lower bounds of the gray or red regions correspond to the upper and
lower quartiles of the drag ratio distributions, respectively. We arrange these 29 solutes in order
of decreasing basal crossover temperature—the temperature at which the median of the drag
ratio becomes zero—from left to right and top to bottom. The interquartile range (IQR)—width
of the shaded regions—is narrow when the drag ratio is near one at low temperatures and the
IQR increases with temperature as it approaches the crossover temperature.

4.6   Conclusion

We develop a computationally efficient methodology based on Bayesian sampling to
quantify uncertainty in the diffusion coefficients and solute drag ratios and apply it
to the vacancy-mediated solute transport in Mg. The uncertainties in DFT energies
due to the exchange-correlation functional are used as a case study. We show that
the solute diffusivities obey a multivariate log-normal distribution across different
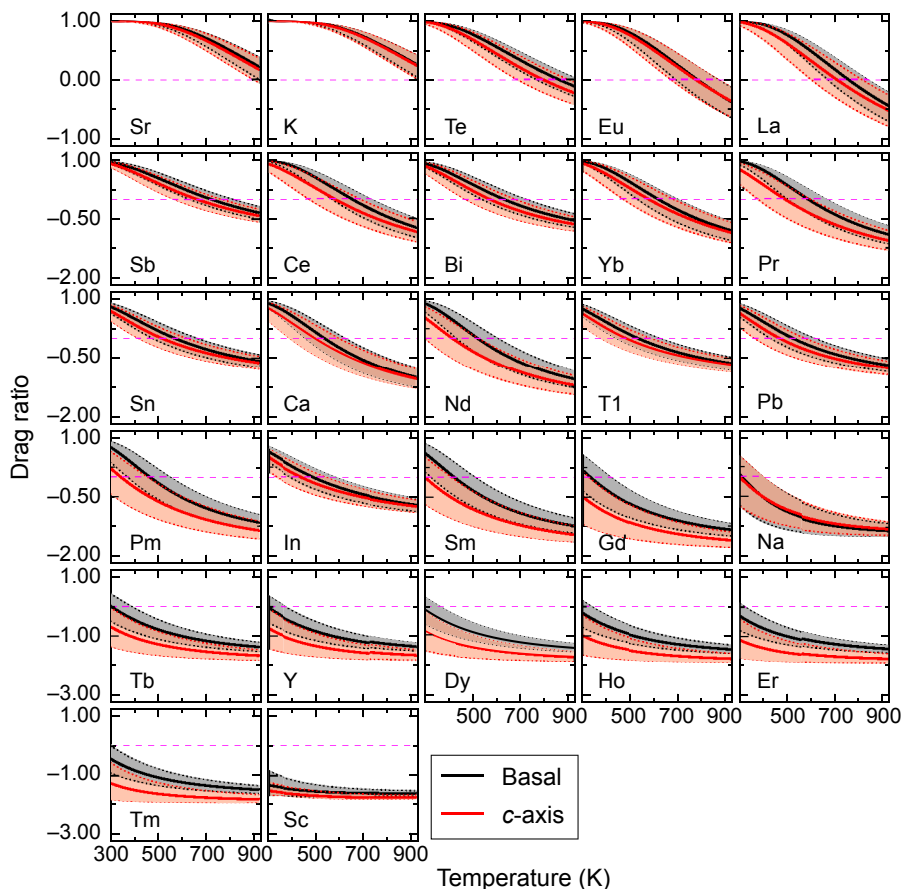
Figure 4.10 Three quartiles of the drag ratio distributions in the basal plane and along the c-axis for solutes where outer ring networks lead to reorientation of the vacancy around the solute. For Sr, K, Te, Eu, La, Sb, Ce, Bi, and Yb, their attractive binding energies of greater than 100 meV with a vacancy coupled with faster outer ring network rates compared to escape rates lead to a narrow distribution of drag ratio at low temperatures. The remaining solutes—Pr to Sc—have smaller attractive or repulsive binding with vacancy which lead to wide distribution of drag ratios at low temperatures. Near crossover temperature, the spread of the drag ratio distribution is maximum and decreases or becomes constant at higher temperatures.

temperatures and compute their covariance matrix using two approaches—a stochastic and a computationally efficient analytical method—which agree well. We quantify uncertainty in Arrhenius parameters through a correlated error fit and find that the standard deviation of the activation energy of diffusion lies between 90 and 120 meV for all the 61 solutes with small uncertainties in diffusion prefactors caused only by changes in dominant diffusion pathways. A nonzero uncertainty in diffusion prefactor for Tl, Pb, Bi, Li, Te, and the first half of the lanthanides indicates that more than one vacancy transition rate dominates in the temperature interval of 300−923K. We find
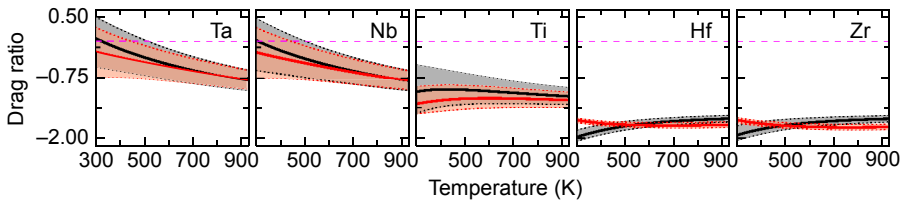
Figure 4.11 Three quartiles of the drag ratio distributions in the basal plane and along the *c*-axis for solutes whose vacancy reorientation rates in inner and outer ring network are similar. These five solutes have high repulsive interactions with vacancy (> 0.2 eV) leading to negative median of drag ratio above 300K except for Ta. The solutes Ta, Nb, and Ti show the maximum spread in drag ratio distribution near 300K because it is the closest temperature to crossover. The spread of the distributions decreases with temperature and becomes constant at higher temperatures for Hf and Zr.

that the experimentally measured diffusivities fall within the computed error bars for most solutes. The drag ratios are not normally distributed and are sensitive to the variation in vacancy reorientation barriers and solute−vacancy binding energies. The IQR quantifies the spread of the drag ratio distributions, and we observe that the IQR is maximum near the crossover temperature, signifying the maximum uncertainty in drag ratio.

Our methodology of uncertainty quantification for solute transport coefficients is general and can be extended to other crystal lattices, such FCC and BCC, as well as to other defect-mediated diffusion such as interstitial mechanisms. In our analysis, we ignore the uncertainty in attempt frequency and defect formation entropies which is expected to have minimal impact on the accuracy of uncertainty quantification of the diffusion prefactors. In the future, the distribution of parameters could be considered using the BEEF exchange-correlation functional and is worth investigation in future studies [80]. Finally, the inclusion of uncertainties in computationally generated transport databases will help to ascertain their reliability and robustness.

References

[1] A.R. Allnatt, A.B. Lidiard, Atomic Transport in Solids, Cambridge University Press, Cambridge, 1993, pp. 202−203. Chap. 5.

[2] R.W. Balluffi, S.M. Allen, W.C. Carter, Kinetics of Materials, John Wiley & Sons, Inc., 2005. ISBN 9780471749318.

[3] H. Wu, T. Mayeshiba, D. Morgan, High-throughput ab-initio dilute solute diffusion database, Sci. Data 3 (2016) 160054.

[4] L. Messina, M. Nastar, N. Sandberg, P. Olsson, Systematic electronic-structure investigation of substitutional impurity diffusion and flux coupling in bcc iron, Phys. Rev. B 93 (2016) 184302.

[5] R. Agarwal, D.R. Trinkle, Ab initio magnesium-solute transport database using exact diffusion theory, Acta Mater. 150 (2018) 339.

[6] T. Garnier, M. Nastar, P. Bellon, D.R. Trinkle, Solute drag by vacancies in body-centered cubic alloys, Phys. Rev. B 88 (2013) 134201.

[7] T. Garnier, D.R. Trinkle, M. Nastar, P. Bellon, Quantitative modeling of solute drag by vacancies in face-centered-cubic alloys, Phys. Rev. B 89 (2014) 144202.

[8] R. Agarwal, D.R. Trinkle, Exact model of vacancy-mediated solute transport in magnesium, Phys. Rev. Lett. 118 (2017) 105901.

[9] B. Medasani, M. Haranczyk, A. Canning, M. Asta, Vacancy formation energies in metals: a comparison of MetaGGA with LDA and GGA exchange−correlation functionals, Comput. Mater. Sci. 101 (2015) 96−107.

[10] S.-L. Shang, B.-C. Zhou, W.Y. Wang, A.J. Ross, X.L. Liu, Y.-J. Hu, H.-Z. Fang, Y. Wang, Z.-K. Liu, A comprehensive first-principles study of pure elements: vacancy formation and migration energies and self-diffusion coefficients, Acta Mater. 109 (2016) 128−141.

[11] D.R. Trinkle, Automatic numerical evaluation of vacancy-mediated transport for arbitrary crystals: onsager coefficients in the dilute limit using a Green function approach, Philos. Mag. 1 (2017). https://doi.org/10.1080/14786435.2017.1340685.

[12] A. Smigelskas, E. Kirkendall, Zinc diffusion in alpha brass, Trans. AIME 171 (1947) 130−142.

[13] G.E. Murch, Simulation of diffusion kinetics with the Monte Carlo method, in: G.E. Murch, A.S. Nowick (Eds.), Diffusion in Crystalline Solids, Academic Press, Orlando, Florida, 1984, pp. 379−427. Chap. 7.

[14] I.V. Belova, G.E. Murch, Collective diffusion in the binary random alloy, Philos. Mag. A 80 (2000) 599−607.

[15] I.V. Belova, G.E. Murch, Behaviour of the diffusion vacancy-wind factors in the concentrated random alloy, Philos. Mag. A 81 (2001) 1749−1758.

[16] I.V. Belova, G.E. Murch, Computer simulation of solute-enhanced diffusion kinetics in dilute fcc alloys, Philos. Mag. 83 (2003) 377−392.

[17] I.V. Belova, G.E. Murch, Solvent diffusion kinetics in the dilute random alloy, Philos. Mag. 83 (2003) 393.

[18] M. Nastar, V.Y. Dobretsov, G. Martin, Self-consistent formulation of configurational kinetics close to equilibrium: the phenomenological coefficients for diffusion in crystalline solids, Philos. Mag. A 80 (2000) 155−184.

[19] M. Nastar, Segregation at grain boundaries: from equilibrium to irradiation induced steady states, Philos. Mag. 85 (2005) 641−647. http://www.tandfonline.com/doi/pdf/10.1080/14786430412331320035.

[20] K.D. Belashchenko, V.G. Vaks, The master equation approach to configurational kinetics of alloys via the vacancy exchange mechanism: general relations and features of microstructural evolution, J. Phys. 10 (1998) 1965−1983.

[21] V.G. Vaks, A.Y. Stroev, I.R. Pankratov, A.D. Zabolotskiy, Statistical theory of diffusion in concentrated alloys, J. Exp. Theor. Phys. 119 (2014) 272−299.

[22] V.G. Vaks, K.Y. Khromov, I.R. Pankratov, V.V. Popov, Statistical theory of diffusion in concentrated BCC and FCC alloys and concentration dependences of diffusion coefficients in BCC alloys FeCu, FeMn, FeNi, and FeCr, J. Exp. Theor. Phys. 123 (2016) 59−85.

[23] R. Kikuchi, The path probability method, Prog. Theor. Phys. Suppl. 35 (1966) 1−64.

[24] H. Sato, R. Kikuchi, Theory of many-body diffusion by the path-probability method: conversion from ensemble averaging to time averaging, Phys. Rev. B 28 (1983) 648−664.

[25] H. Sato, T. Ishikawa, R. Kikuchi, Correlation factor in tracer diffusion for high tracer concentrations, J. Phys. Chem. Solids 46 (1985) 1361−1370.

[26] E.W. Montroll, G.H. Weiss, Random walks on lattices. II, J. Math. Phys. 6 (1965) 167−181.

[27] M. Koiwa, S. Ishioka, Integral methods in the calculation of correlation factors for impurity diffusion, Philos. Mag. A 47 (1983) 927−938.

[28] D.R. Trinkle, Diffusivity and derivatives for interstitial solutes: activation energy, volume, and elastodiffusion tensors, Philos. Mag. 96 (2016) 2714−2735. https://doi.org/10.1080/14786435.2016.1212175.

[29] Z.W. Gortel, M.A. Załuska-Kotur, Chemical diffusion in an interacting lattice gas: analytic theory and simple applications, Phys. Rev. B 70 (2004) 125431.

[30] M.A. Załuska-Kotur, Z.W. Gortel, Ritz variational principle for collective diffusion in an adsorbate on a non-homogeneous substrate, Phys. Rev. B 76 (2007) 245401.

[31] M.A. Załuska-Kotur, Variational approach to the diffusion on inhomogeneous lattices, Appl. Surf. Sci. 304 (2014) 122−126.

[32] D.R. Trinkle, Variational principle for mass transport, Phys. Rev. Lett. 121 (2018) 235901.

[33] P.B. Ghate, Screened interaction model for impurity diffusion in Zinc, Phys. Rev. 133 (1964) A1167−A1175.

[34] A.P. Batra, Anisotropic isotope effect for diffusion of zinc and cadmium in zinc, Phys. Rev. 159 (1967) 487−499.

[35] A. Allnatt, I. Belova, G. Murch, Diffusion kinetics in dilute binary alloys with the h.c.p.crystal structure, Philos. Mag. 94 (2014) 2487−2504.

[36] S.L. Shang, L.G. Hector, Y. Wang, Z.K. Liu, Anomalous energy pathway of vacancy migration and self-diffusion in hcp Ti, Phys. Rev. B 83 (2011) 224104.

[37] W.W. Xu, S.L. Shang, B.C. Zhou, Y. Wang, L.J. Chen, C.P. Wang, X.J. Liu, Z.K. Liu, A first-principles study of the diffusion coefficients of alloying elements in dilute α-Ti alloys, Phys. Chem. Chem. Phys. 18 (2016) 16870−16881.

[38] G. Vérité, F. Willaime, C.-C. Fu, Anisotropy of the vacancy migration in Ti, Zr and Hf hexagonal close-packed metals from first principles, in: Solid State Phenomena, vol. 129, 2007, pp. 75−81.

[39] G.H. Vineyard, Frequency factors and isotope effects in solid state rate processes, J. Phys. Chem. Solids 3 (1957) 121−127.

[40] G. Strang, The finite element method and approximation theory, in: B. Hubbard (Ed.), Numerical Solution of Partial Differential Equations−II, Academic Press, 1971, pp. 547−583.

[41] D.R. Trinkle, Onsager, 2017. http://dallastrinkle.github.io/Onsager.

[42] G. Kresse, J. Furthmüller, Efficient iterative schemes for *ab initio* total-energy calculations using a plane-wave basis set, Phys. Rev. B 54 (1996) 11169−11186.

[43] P.E. Blöchl, Projector augmented-wave method, Phys. Rev. B 50 (1994) 17953−17979.

[44] G. Kresse, D. Joubert, From ultrasoft pseudopotentials to the projector augmented-wave method, Phys. Rev. B 59 (1999) 1758−1775.

[45] M. Methfessel, A.T. Paxton, High-precision sampling for brillouin-zone integration in metals, Phys. Rev. B 40 (1989) 3616−3621.

[46] G. Henkelman, B.P. Uberuaga, H. Jónsson, A climbing image nudged elastic band method for finding saddle points and minimum energy paths, J. Chem. Phys. 113 (2000) 9901−9904.

[47] J.P. Perdew, A. Zunger, Self-interaction correction to density-functional approximations for many-electron systems, Phys. Rev. B 23 (1981) 5048−5079.

[48] J.P. Perdew, K. Burke, M. Ernzerhof, Generalized gradient approximation made simple, Phys. Rev. Lett. 77 (1996) 3865−3868.

[49] J.P. Perdew, Y. Wang, Accurate and simple analytic representation of the electron-gas correlation energy, Phys. Rev. B 45 (1992) 13244−13249.

[50] J.P. Perdew, A. Ruzsinszky, G.I. Csonka, O.A. Vydrov, G.E. Scuseria, L.A. Constantin, X. Zhou, K. Burke, Restoring the density-gradient expansion for exchange in solids and surfaces, Phys. Rev. Lett. 100 (2008), 136406−11366.

[51] J. Sun, R.C. Remsing, Y. Zhang, Z. Sun, A. Ruzsinszky, H. Peng, Z. Yang, A. Paul, U. Waghmare, X. Wu, M.L. Klein, J.P. Perdew, Accurate first-principles structures and energies of diversely bonded systems from an efficient density functional, Nat. Chem. 8 (2016). https://doi.org/10.1038/nchem.2535.

[52] J. Friis, G.K.H. Madsen, F.K. Larsen, B. Jiang, K. Marthinsen, R. Holmestad, Magnesium: comparison of density functional theory calculations with electron and x-ray diffraction experiments, J. Chem. Phys. 119 (2003) 11359−11366.

[53] C. Janot, D. Malléjac, B. George, Vacancy-formation energy and entropy in magnesium single crystals, Phys. Rev. B 2 (1970) 3088−3098.

[54] P. Tzanetakis, J. Hillairet, G. Revel, Formation of energy of vacancies in aluminium and magnesium, Phys. Status Solidi B 75 (1976) 433−439.

[55] C. Mairy, J. Hillairet, D. Schumacher, Energie de formation et concentration d'équilibre des lacunes dans le magnésium, Acta Metall. 15 (1967) 1258−1261.

[56] J. Delaplace, J. Hillairet, J.C. Nicoud, D. Schumacher, G. Vogl, Low temperature neutron radiation damage and recovery in magnesium, Phys. Status Solidi B 30 (1968) 119−126.

[57] J. Combronde, G. Brebec, Anisotropie d'autodiffusion du magnésium, Acta Metall. 19 (1971) 1393−1399.

[58] R. Agarwal, D.R. Trinkle, Data Citation: Solute Transport Database in Mg Using Ab Initio and Exact Diffusion Theory, 2017. https://doi.org/10.18126/M20G83.

[59] K. Kroeze, Multidimensional Gauss-Hermite Quadrature in R, 2014. https://github.com/Karel-Kroeze/MultiGHQuad.

[60] K. Lal, Study of the Diffusion of Some Elements in Magnesium, CEA Report R-3136, 1967, p. 54.

[61] W. Zhong, J.-C. Zhao, First experimental measurement of calcium diffusion in magnesium using novel liquid-solid diffusion couples and forward-simulation analysis, Scr. Mater. 127 (2017) 92−96.

[62] M. Paliwal, S.K. Das, J. Kim, I.-H. Jung, "Diffusion of Nd in hcp Mg and interdiffusion coefficients in Mg−Nd system, Scr. Mater. 108 (2015) 11−14.

[63] S.K. Das, Y.-B. Kang, T. Ha, I.-H. Jung, Thermodynamic modeling and diffusion kinetic experiments of binary Mg−Gd and Mg−Y systems, Acta Mater. 71 (2014) 164−175.

[64] J. Combronde, G. Brebec, Heterodiffusion de Ag, Cd, In, Sn et Sb dans le magnésium, Acta Metall. 20 (1972) 37−44.

[65] W. Zhong, J.-C. Zhao, First measurement of diffusion coefficients of lithium in magnesium, Private Communication (December 2019).

[66] J. Čermák, I. Stloukal, Diffusion of ^{65}Zn in Mg and in Mg-x Al solid solutions, Phys. Status Solidi A 203 (2006) 2386−2392.

[67] S.K. Das, Y.-M. Kim, T.K. Ha, I.-H. Jung, "Investigation of anisotropic diffusion behavior of Zn in hcp Mg and interdiffusion coefficients of intermediate phases in the Mg−Zn system, Calphad 42 (2013) 51−58.

[68] C. Kammerer, N. Kulkarni, R. Warmack, Y. Sohn, Interdiffusion and impurity diffusion in polycrystalline Mg solid solution with Al or Zn, J. Alloy. Comp. 617 (2014) 968−974.

[69] W. Zhong, J.-C. Zhao, First reliable diffusion coefficients for Mg-Y and additional reliable diffusion coefficients for Mg-Sn and Mg-Zn, Metall. Mater. Trans. A 48 (2017) 5778−5782.

[70] I. Stloukal, J. Čermák, Grain boundary diffusion of 67ga in polycrystalline magnesium, Scr. Mater. 49 (2003) 557−562.

[71] V. Yerko, V. Zelenskiy, V. Krasnorustskiy, Diffusion of beryllium in magnesium, Phys. Met. Metallogr. 22 (1966) 112−114.

[72] S. Brennan, A.P. Warren, K.R. Coffey, N. Kulkarni, P. Todd, M. Kilmov, Y. Sohn, Aluminum impurity diffusion in magnesium, J. Phase Equilib. Diffus. 33 (2012) 121−125.

[73] S. Brennan, K. Bermudez, N.S. Kulkarni, Y. Sohn, Interdiffusion in the Mg-Al system and intrinsic diffusion in β-Mg$_2$Al$_3$, Metall. Mater. Trans. A 43 (2012) 4043−4052.

[74] S.K. Das, Y.-M. Kim, T.K. Ha, R. Gauvin, I.-H. Jung, Anisotropic diffusion behavior of Al in Mg: diffusion couple study using Mg single crystal, Metall. Mater. Trans. A 44 (2013) 2539−2547.

[75] S.K. Das, Y.-M. Kim, T.K. Ha, R. Gauvin, I.-H. Jung, Erratum to: anisotropic diffusion behavior of Al in Mg: diffusion couple study using Mg single crystal, Metall. Mater. Trans. A 44 (2013) 3420−3422.

[76] J. Dai, B. Jiang, J. Zhang, Q. Yang, Z. Jiang, H. Dong, F. Pan, Diffusion kinetics in Mg-Cu binary system, J. Phase Equilib. Diffus. 36 (2015) 613−619.

[77] S. Fujikawa, Impurity diffusion of manganese in magnesium, J. Jpn. Inst. Light Metals 42 (1992) 826−827.

[78] L. Pavlinov, A. Gladyshev, V. Bykov, Self-diffusion in calcium and diffuse of barely soluble impurities in magnesium and calcium, Phys. Met. Metallogr. 26 (1968) 53−59.

[79] D. Xiu, Stochastic collocation methods: a survey, in: R. Ghanem, D. Higdon, H. Owhadi (Eds.), Handbook of Uncertainty Quantification, Springer, 2015, pp. 1−18.

[80] J. Wellendorff, K.T. Lundgaard, A. Møgelhoj, V. Petzold, D.D. Landis, J.K. Norskov, T. Bligaard, K.W. Jacobsen, Density functionals for surface science: exchange-correlation model development with bayesian error estimation, Phys. Rev. B 85 (2012) 235149.